

Pyroelectric Crystal-Based X-Ray Diffractometer

by

Louis Edward Fernandes

Submitted to the Department of Physics
in partial fulfillment of the requirements for the degree of
Bachelor of Science

at the

MASSACHUSETTS INSTITUTE OF TECHNOLOGY

June 2007

© Louis Edward Fernandes, MMVII. All rights reserved.

The author hereby grants to MIT permission to reproduce and
distribute publicly paper and electronic copies of this thesis document
in whole or in part.

Author *Louis Edward Fernandes*

Department of Physics

May 11, 2007

Certified by *David G. Cory*

David G. Cory

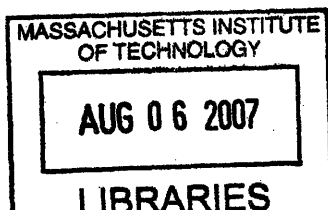
Professor

Thesis Supervisor, Department of Nuclear Science and Engineering

Accepted by *David E. Pritchard*

Professor David E. Pritchard

Senior Thesis Coordinator, Department of Physics



ARCHIVES

Pyroelectric Crystal-Based X-Ray Diffractometer

by

Louis Edward Fernandes

Submitted to the Department of Physics
on May 11, 2007, in partial fulfillment of the
requirements for the degree of
Bachelor of Science

Abstract

We investigate the use of an Amptek Cool-X X-ray Generator for an instructional tool in the physics of x-rays, as well as a source for x-rays for crystal diffraction experiments. The x-ray source is a solid-state two-phase air-cooled source with a time-varying photon output. Two detectors are used in this experiment, the first being an Amptek X-123 Spectrometer and the second a combination scintillator/Polaroid film setup. We collimate the x-ray beam and determine that the system, although low flux and low resolution, will function as a quick and easy tool for the investigation of x-ray physics.

Thesis Supervisor, Department of Nuclear Science and Engineering: David G. Cory
Title: Professor

Acknowledgments

The author would like to thank his thesis advisor, Professor David G. Cory, for the immense amount of support, advice, and patience given during the course of the thesis work. The author would also like to thank Dr. Chandrasekhar Ramanathan for his assistance with the experimental apparatus and the use of the crystals examined, without which this document would not be possible. Thanks are also due to Peter Allen, who machined all of the homemade parts for this experiment. The author also is grateful for the assistance of Gheorghe Chistol and the MIT *Technique* for the loan of the Polaroid Land film holder and the generous donation of some of the Polaroid film used. This work was supported financially by MIT Nuclear Science and Engineering department course development and discretionary funds.

Contents

1	Introduction	11
2	Cool-X X-ray Source	13
2.1	X-ray Production	13
2.2	The Collimator	16
2.3	Collimator Attenuation	17
2.4	Source Distribution	20
2.5	Intensity Reduction from Collimation	21
3	X-ray Detection	23
3.1	X-123 Spectrometer	23
3.2	Polaroid Film	24
3.3	Phosphor Screen	25
4	Crystallographic Considerations	29
4.1	Crystal Basics	29
4.2	Bragg Equation	30
4.3	Methods of Diffraction	33
5	Results	37
5.1	Experimental Setup	37
5.2	Experimental Procedure	39
5.3	Experimental Results	40

6	Conclusions	43
A	Bragg Interference	45

List of Figures

2-1	A schematic of the Cool-X x-ray source. Image courtesy Amptek, Inc.	14
2-2	The output spectra of the Cool-X x-ray source.	15
2-3	Energy level diagrams of the $K\alpha$ 2-3(a) and the $K\beta$ 2-3(b) lines. Energy of emission given below diagrams.	15
2-4	Diagram of the collimator design for the Cool-X x-ray source. Figure not to scale.	16
2-5	Diagram to illustrate variables used in intensity calculation.	18
2-6	Angular intensity distribution of the Cool-X source. Figure courtesy Amptek, Inc.	21
3-1	A screenshot of the Amptek ADMCA computer interface, showing an uncollimated point-blank exposure of the XR-100CR detector to the Cool-X source.	24
4-1	Diagram to illustrate variables used in the derivation of Bragg scattering.	31
4-2	Different methods of x-ray diffraction.	34
5-1	Picture of the desktop setup for the experiments. Seen are the collimated Cool-X source, the X-123 spectrometer, and the goniometer mount in back.	40
5-2	Sample exposures of Polaroid type 59 film to the Cool-X source. All figures are at the same scale.	41
A-1	Parallel x-ray scattering off of three lattice points.	46
A-2	Lattice plane RS reflection.	46

Chapter 1

Introduction

The Cool-X X-ray Generator (Cool-X)[2] is a thermoelectrically cooled solid state x-ray generator. Although this source is small and low-flux ($\approx 10^8$ photons/sec), it is an attractive x-ray source for many applications. Low-flux sources are ideal in an educational environment, as they are easier to shield than their larger, more powerful counterparts. We will be investigating the use of the Cool-X as a low-flux x-ray source for use in an academic setting as a tool for illustrating x-ray physics and diffraction phenomena, such as Bragg diffraction.

In Chapter 2, we will discuss the properties of the Cool-X source and the methods used to collimate the x-rays produced.

In Chapter 3, we will examine the various methods available to us for x-ray detection. We will examine the properties of the X-123 Spectrometer and XR-100CR detector, as well as discuss phosphor screens and Polaroid film recording devices.

Chapter 4 contains a discussion on the properties of crystal systems and the Bragg equation, what could be called the most important equation in x-ray diffraction.

In Chapter 5 we discuss the experimental procedure used to acquire acquire film exposures utilizing our collimated x-ray source. We show the results obtained after exposure.

Chapter 6 concludes our discussion and summarizes the next steps necessary in using the Cool-X source as a diffractometer.

Chapter 2

Cool-X X-ray Source

2.1 X-ray Production

The heart of any x-ray system is the x-ray source. For many x-ray experiments, sources such as synchrotrons, linear accelerators, rotating-anode tubes, and flash tubes are employed for reasons including the ability to tune the radiation to a specific wavelength, the need for a very large flux for long periods of time, or the need for a very short-lived pulse of x-rays [4].

The x-ray source discussed here possesses a different mode of operation. The Cool-X X-ray source, developed and distributed by Amptek, Inc., uses a pyroelectric crystal to generate x-rays [2]. Pyroelectric crystals, such as LiTaO_3 or LiNbO_3 , react to a change in temperature at an appropriate pressure by creating an electric field that, in a semi-vacuum system, will drive electrons in the gas away from the crystal and into a target. The electrons will then stop within the target, emitting characteristic x-rays on top of a bremsstrahlung spectrum. The crystal is also mounted on a Cu seat, such that when the heating elements heat the crystal, electrons are driven towards the Cu target, and during cool-down, electrons are driven at the Cu seat. We see the $K\alpha$ and the $K\beta$ peaks quite clearly above the bremsstrahlung spectrum, as shown in Figure 2-2. If you cycle the heating and cooling of this crystal, what emerges is a time-changing x-ray flux that is characteristic of the target material. This flux is emitted from the target isotropically. See Figure 2-1 for further elaboration.

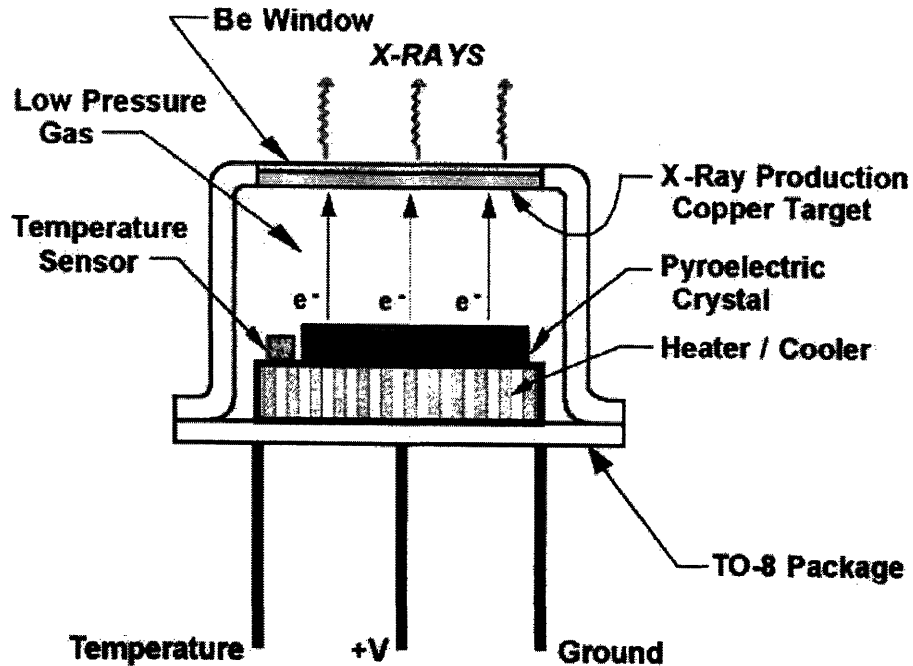
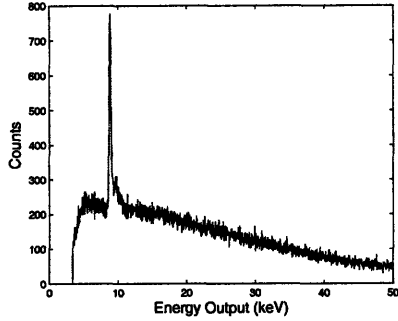


Figure 2-1: A schematic of the Cool-X x-ray source. Image courtesy Amptek, Inc.

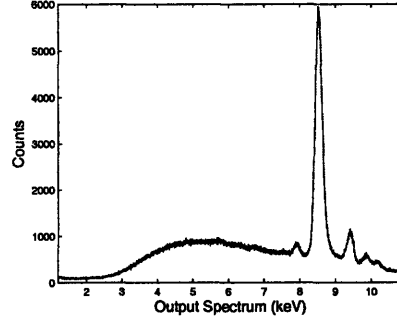
The source employed during this work utilizes a Cu target for generation of x-rays. We must be careful not to run the source for too long, as continued use can damage the crystal elements in the source, resulting in a decrease in flux. We kept the exposure time to under an hour and a half per day, as Amptek has advised [2], will be made.

The $K\alpha$ line we see in Figure 2-2 at 8.04 keV with a FWHM of 0.20 keV is actually a superposition of two peaks of lesser intensity, the $K\alpha_1$ and $K\alpha_2$ lines, which have relative intensities compared to the peak of the spectrum of 0.94 and 0.34 respectively [5]. Figure 2-2(b) does not have the resolution to see this peak separation, since the detector employed has a FWHM of ≈ 150 eV. The $K\beta$ line at 8.90keV with a FWHM of 0.13 keV is likewise composed of multiple lines, in this case, five, but again, our system doesn't have the resolution to observe this. Figure 2-3 diagrams the transitions that give rise to the $K\alpha$ and $K\beta$ lines.

The source is internally collimated, in that the housing for the apparatus absorbs all of the x-rays that are not emitted through the window. The window is a 250

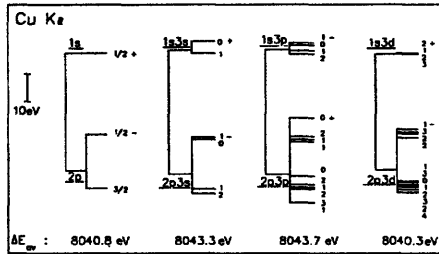


(a) Output spectrum of the Cool-X x-ray source. Note the bremsstrahlung curve accentuated by the $K\alpha$ and $K\beta$ lines.

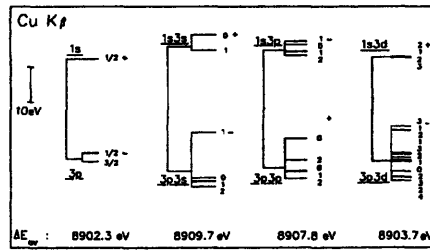


(b) The low-energy portion of the Cool-X source. Note the $K\alpha$ peak at 8.04keV with with of 0.20keV and the $K\beta$ peak at 8.90keV with a width of 0.13keV.

Figure 2-2: The output spectra of the Cool-X x-ray source.



(a)



(b)

Figure 2-3: Energy level diagrams of the $K\alpha$ 2-3(a) and the $K\beta$ 2-3(b) lines. Energy of emission given below diagrams.

μm thick pure Be window. This window allows the transmission of x-rays from the target to the outside world, while maintaining a semi-vacuum and minimizing the attenuation of the Cu $K\alpha$ and $K\beta$ radiation. The profile resulting from this collimation is discussed in Section 2.4. The collimation resulting from the housing is insufficient for the purposes of crystallography, as it is widely divergent, but the addition of a second collimation stage will help make the beam more suitable to our purposes.

2.2 The Collimator

The object of our collimator is to make the x-rays as parallel as realistically possible upon exiting the collimator. We require this as a condition for crystallography; it is possible to do crystallography with divergent beams, but the more divergent the beam, the more “smearing” of the diffraction pattern occurs.

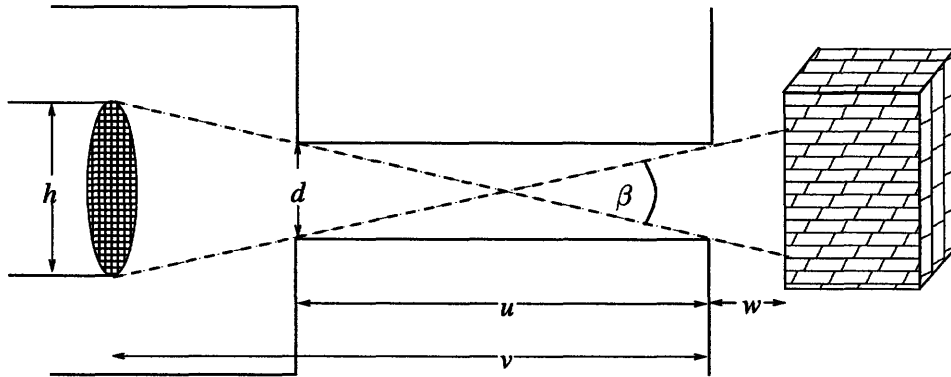


Figure 2-4: Diagram of the collimator design for the Cool-X x-ray source. Figure not to scale.

Figure 2-4 demonstrates the setup for our collimator. We have chosen a collimator scheme where convergent beams from the edges of the source cross at the center of the collimator. The maximum angle of divergence, β , for small β is

$$\tan \beta \approx \beta = \frac{2d}{u} \quad (2.1)$$

However, to use this setup, we have a constraint on the geometry, as Equation 2.1

immediately implies that

$$\tan \beta \approx \beta = \frac{h}{v - u/2} = \frac{2d}{u} \Rightarrow h = d \left(\frac{2v}{u} - 1 \right) \quad (2.2)$$

which gives us the conditions our dimensions must adhere to in order to use our formula for the maximum divergence angle of our extended source.

Another consideration for this collimator is that we are attenuating the beam considerably if we want to decrease the divergence of the beam to a level where $\tan \beta$ is small enough to be $\approx \beta$. If our source was a point source, we could easily calculate this; we would have a spherical wavefront propagating out of our source, and so the intensity would only decrease by the ratio of $\frac{d^2}{r^2}$. However, our source is not nearly a point source, and so we must do more work to get a more accurate value for the intensity after collimation.

2.3 Collimator Attenuation

We will begin the analysis of our extended source, like [8], with a generic source intensity distribution, $s(x_s, y_s)$ and detector intensity $I_d(x_d, y_d)$ where (x_s, y_s) and (x_d, y_d) represent the source and detector coordinates respectively. We insert a generalized collimator in between source and detector and give it a space-dependent attenuation coefficient $\mu_o(x, y, z)$ with general space coordinates. See Figure 2-5 for clarification.

An infinitesimal projection of the source intensity $s(x_s, y_s)$ on the detector plane, neglecting any attenuation, has the form of

$$dI_i(x_d, y_d) = dI_0 \cos^3 \theta \quad (2.3)$$

The $\cos^3 \theta$ dependence can be interpreted as such: we get one factor of $\cos \theta$ from the obliqueness of a projected circle on the detector area, and a factor of $\cos^2 \theta$ from the $\frac{1}{r^2}$ dependence of the increasing infinitesimal spherical wavefront propagating from the source element. For further detail see [3, 8].

We define dI_0 as being the infinitesimal intensity element on the axis such that

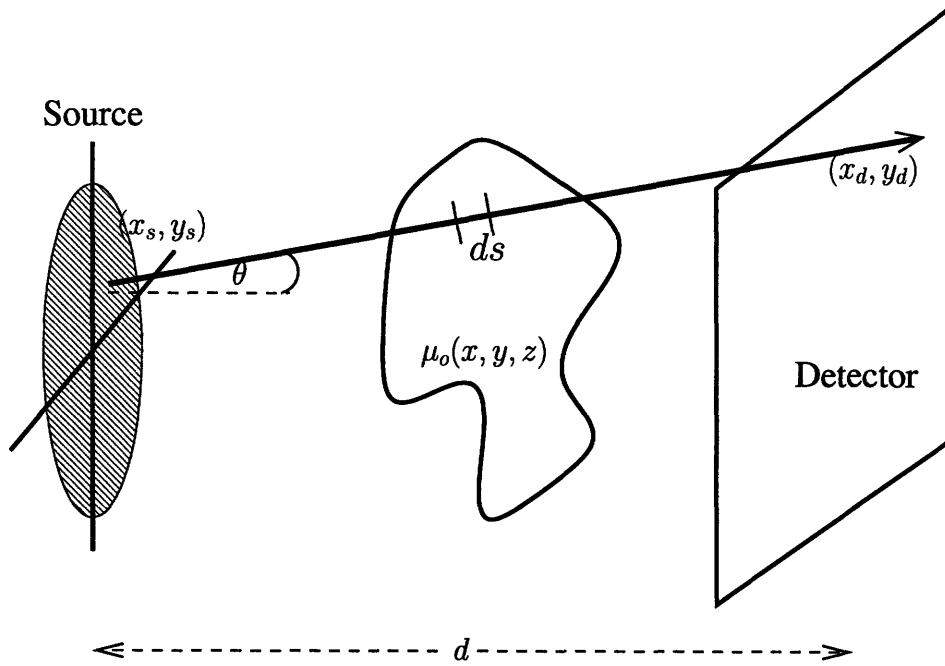


Figure 2-5: Diagram to illustrate variables used in intensity calculation.

$x_s = x_d, y_s = y_d$ such that

$$dI_0 = \frac{s(x_s, y_s) dx_s dy_s}{4\pi d^2} \quad (2.4)$$

We now look for a way to write $\cos^3 \theta$ in terms of the position variables so we can do an integration in Cartesian space. We find the simple trigonometric relationship

$$\cos \theta = \frac{d}{\sqrt{d^2 + (x_d - x_s)^2 + (y_d - y_s)^2}} \Rightarrow \cos^3 \theta = \frac{1}{\sqrt{1 + \frac{(r_{ds}^2)}{d^2}}}^3 \quad (2.5)$$

where $r_{ds}^2 = (x_d - x_s)^2 + (y_d - y_s)^2$.

If all our system was the source and the detector, this would be a very good first order attempt at modeling the system. However, we have a collimator, which we provided for by inserting the general object into our system (see Figure 2-5). We will insert a general object into our path before specifying that we have a collimator and not a malformed blob.

Our detector intensity now takes on the form

$$dI_d = dI_s \exp - \int \mu_0(x, y, z) dl \quad (2.6)$$

where $dl = \sqrt{dx^2 + dy^2 + dz^2} = dz\sqrt{1 + \left(\frac{dx}{dz}\right)^2 + \left(\frac{dy}{dz}\right)^2}$. It would simplify our computation immensely if we changed our coordinates from (x, y) to (x_s, y_s) or (x_d, y_d) , and so we'll parameterize our equation with

$$x = \frac{x_d - x_s}{d}z + x_s \text{ and } y = \frac{y_d - y_s}{d}z + y_s \quad (2.7)$$

This parametrization comes from writing down the equation of the line that our infinitesimal source element is shining through. This is also seen through magnification effects on the object and the source [8]. Substituting our parametrization back into Equation 2.6 and integrating over the source and detector variables we are left with the following:

$$\begin{aligned} I_d(x_d, y_d) &= \int dI_d(x_s, y_s, x_d, y_d) \\ &= \frac{1}{4\pi d^2} \iint \frac{s(x_s, y_s)}{\sqrt{1 + \left(\frac{r_{ds}}{d}\right)^2}^3} \dots \\ &\quad \exp \left[-\sqrt{1 + \left(\frac{r_{ds}}{d}\right)^2} \int \mu_0 \left(\frac{x_d - x_s}{d}z + x_s, \frac{y_d - y_s}{d}z + y_s \right) dz \right] \end{aligned} \quad (2.8)$$

Equation 2.8 gives us a straightforward method of computing the intensity on the entire detector surface, given a model of the object we are examining. In our case, we are examining a collimator, so we can construct a model of this collimator and insert it into our equation to get a numerical estimate of the attenuation due to the collimator.

Our collimator simulation is fairly straightforward. The collimator is basically a hole surrounded by a high absorption rate material (Al, in our case). This is easy to implement in a numerical situation, and can be added easily into the integration that occurs to get $I_d(x_d, y_d)$.

Another approach, which yields the same answer, involves analyzing a point source as the x-ray travels through a series of infinitely thin sheets on the z -axis. This approach naturally leads us to a convolutional representation of our intensity of the form

$$I_d(x_d, y_d) = \frac{1}{4\pi d^2 m^2} s\left(\frac{x_d}{m}, \frac{y_d}{m}\right) * \exp\left(-\tau\left(\frac{x_d}{M}, \frac{y_d}{M}\right)\right) \quad (2.9)$$

where τ is defined by

$$\mu_0(x, y, z) = \tau(x, y)\delta(z - z_0) \quad (2.10)$$

with $m = \frac{-(d-z)}{z}$ and $M = \frac{d}{z}$.

The same model we made for $\mu_0(x, y, z)$ would suffice for this computation, with a slight change to account for the delta function in z . For our purposes, both equations are equivalent in terms of coding, and so the prior method of direct integration is used.

2.4 Source Distribution

The source distribution $s(x_s, y_s)$ is crucial to the calculation of our intensity distribution $I_d(x_d, y_d)$. If we had a simple point source, as explained in 2.2, we would have a delta function source that would eliminate the need for our integration. However, due to the non-point distribution of our source, we must be very careful about how we model it.

It would be simplest for our simulation model if the surface of our source emitted uniformly and isotropically, as we could then simply insert a uniform intensity for our function $s(x_s, y_s)$ and be done with it. We should expect the radiation to be emitted isotropically, as the processes going on inside of the Cu target producing radiation (bremsstrahlung emission, absorption and re-emission as $K\alpha$ lines, etc.) are all occurring isotropically throughout the target.

As seen in Figure 2.4, the output of the Cool-x is fairly uniform through a 180 degree arc in front of the source, with a fairly sharp drop-off at the edges. This

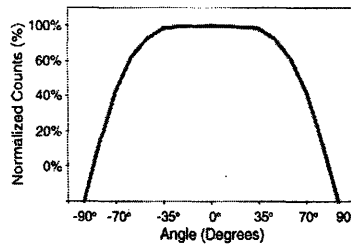


Figure 2-6: Angular intensity distribution of the Cool-X source. Figure courtesy Amptek, Inc.

fits with what we predict well; as in Figure 2-1, the target is located behind the Be window and enclosed by an aluminum housing. This housing prevents x-rays from leaking out any other way than through the Be window, and the short neck of the housing also cuts off low-angle radiation from the source.

What we see across the face of the Cool-x is an uniform output, which is what we expect when being directly in front of an extended source. We see that our assumption of isotropism for the creation of our x-rays is not a bad assumption.

This implies that we can approximate our source function $s(x_s, y_s)$ as uniformly projecting in the forward direction. While the edges of our source might be less than the middle in terms of intensity, the elements at the edges of the source will ultimately contribute far less to the overall intensity of the spot at the end of the collimator, and thus the defects can be ignored for our first-order approximation.

2.5 Intensity Reduction from Collimation

Using our newly acquired $s(x_s, y_s)$ in Equation 2.8, we can now analyze this function for our particular experimental setup. Although this function may not have a nice analytical solution, it is a straightforward matter of numerical calculation. Using Matlab, we can write a simulation that will compute the intensity $I_d(x_d, y_d)$ on a plane at the end of our collimator. The limiting factor of our resolution is the compute time needed per operation, as numerical calculation requires integration across five variables. We shall use measured fluxes for our experiment in place of Equation 2.8.

Chapter 3

X-ray Detection

3.1 X-123 Spectrometer

The device used in this experiment to measure the output spectrum of the Cool-X source is an Amptek X-123 Spectrometer coupled with an XR-100CR detector. The X-123 acts as a multi-channel analyzer (MCA), interfacing with a PC for the XR-100CR element. Figure 3.1 shows the software interface that was used to acquire data and calibrate the spectra. Calibration was achieved through identifying the prominent $K\alpha$ and $K\beta$ lines of the Cool-X. These points were used to linearly fit the MCA bins with energy values.

The XR-100CR detector is a 680 μm thick Si detector, maintained in a vacuum by a Be window 5 mm in radius and 1 mil (25.4 μm) thick [1]. The detector has a maximum resolution of 149 eV, as measured from the FWHM of the 5.9 keV emission of ^{55}Fe . This spreading of a definite energy peak is due mostly to bremsstrahlung interactions in the Be window, and limits just how precisely we can know the energy peaks detected for calibration. The measured peaks were significantly wider than the system resolution.

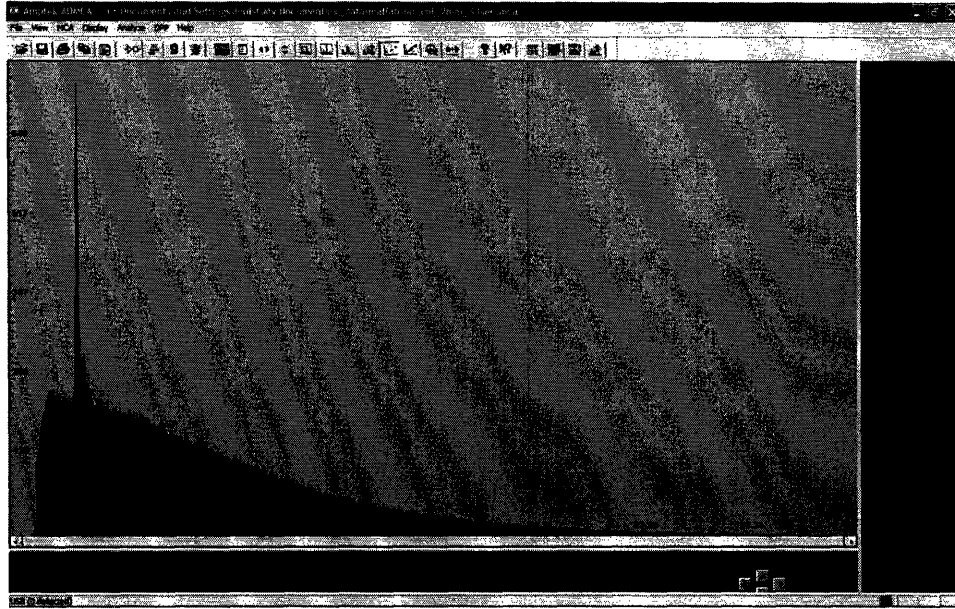


Figure 3-1: A screenshot of the Amptek ADMCA computer interface, showing an uncollimated point-blank exposure of the XR-100CR detector to the Cool-X source.

3.2 Polaroid Film

Polaroid film has been used in x-ray diffraction studies since the 1960's [10, 12] for their speed and simplicity of use. Polaroid film, in combination with a film cassette, takes around a minute to develop, with no additional stopping or fixing agents necessary. Because the film is easy to expose and to process, it is an ideal candidate for rapidly obtaining images. Wet process film takes much longer than Polaroid film, up to nearly an hour, in some cases [10], and requires precise timing of numerous chemical baths in order to get the correct amount of contrast from the film.

Although Polaroid film is designed to be used in the visible spectrum, it will expose upon direct exposure to x-rays. Because the film is optimized for exposure to the visible spectrum, however, the rate at which exposure occurs is not very high. See Figure 5-2 for examples of x-ray exposures of Type 59 Polacolor ER film.

3.3 Phosphor Screen

As shown in Figure 5-2, simply exposing the film as it is to x-rays will not result in a very high contrast. We could expose the film for longer, in order to increase this contrast, but for the reasons covered in Section 2.1, we must limit the time the source operates. So we are left at an impasse. We need more signal from our source than what we are getting, but we can't run our source any longer than we are. We must use a phosphor screen.

Phosphor screens have been in use in x-ray studies since Röntgen first noticed a powder glowing in the vicinity of an evacuated tube with a heated filament in it [11]. And we shall use this same idea to assist in getting a better signal out of our system. Because our film is designed for the visible spectrum and not for x-ray energies, it would behoove us to convert these x-rays into visible photons. And this is exactly what our phosphor will do.

Phosphor screens function, in the energy range that our source produces, through the photoelectric effect. X-rays strike the surface of the phosphor, traveling through and interacting. As these x-rays interact with the lattice of the phosphor, they can knock electrons out of the valence band, giving them enough energy to tunnel through any band gaps present to a conducting band, where they interact with other electrons, the lattice, and the holes formed by the x-rays. As these holes are filled by electrons within the valence band, they emit γ radiation [9]. This radiation is emitted isotropically, with half of the radiation going towards our film. Some of this light will be absorbed as it travels through the medium, but some of it, especially the light near the exiting edge of the powder, will escape and strike our film.

This phosphor screen adds in another limit on our system resolution. Instead of being limited only by the grain size and absorption characteristics of the film, we are now also limited by the resolution introduced by our scintillator. We can model the emission of a visible photon as a spherically symmetric point source emitting a single photon in some direction. As this is not radiating an uniform intensity over all space, but is spitting out discrete photons, we must assign our system a resolution

relative to some standard. We define η_{phos} as the distance away from the axis formed between a radiating point in the scintillator and the recording plane. η_{phos} is the radius of the circle that encloses the area on the detecting plane where $\frac{1}{2}$ of the forward-emitted photons impinge. This is characterized by $\tan \phi = \frac{\eta_{phos}}{l}$ where l is the distance between the phosphor and the recording plane. By defining η_{phos} in this manner, we have characterized an average resolution of our system. Here we have made the approximation that all photons are emitted from a single distance l from the screen, but as long as the thickness t_{phos} of the phosphor obeys $t_{phos} \ll l$ then we can make this assumption.

Where in t_{phos} our photons are emitted is another interesting question. Every phosphor has a peak wavelength of emission; ours will be in the visible spectrum, around 540 nm. This corresponds to an energy of roughly 20 eV, low enough so that any light emitted on the source side of the phosphor will be absorbed before it can escape and hit the recording plane. In order to avoid this problem, our phosphor is designed so that the energy band gap will be sufficiently large that the excited photons do not cause any further excitation of the crystals of the phosphor and have a better chance at escaping. Even so, there will be some attenuation of our emitted light, and so knowing where most of the light is emitted is crucial to determining how much light we get out of the system.

The linear attenuation coefficient can be most precisely found by solving the Dirac equation for the orbital electrons moving a static Hartree-Slater potential [6], but that goes well beyond the scope of this project. Instead, we can approximate the linear attenuation coefficient in the following manner.

The three largest contributors to x-ray attenuation are the photoelectric effect, Rayleigh scattering, and Compton scattering. Our linear mass attenuation coefficient can be written as $\mu = \mu_{PE} + \mu_R + \mu_C$. These coefficients can be written as experimentally fit functions of energy, atomic number Z , and density ρ :

$$\mu = \rho N_g \left[f(E) + C_R \frac{Z^k}{E^l} + C_P \frac{Z^m}{E^n} \right] \quad (3.1)$$

where $N_g = N_A \frac{Z}{A}$ is the electron mass density in electrons per gram, C_R and C_P are constants with a value of 1.25×10^{-24} and 9.8×10^{-24} respectively, E is the energy of our x-ray, k, l, m , and n are constants with the values of 2.0, 1.9, 3.8 and 3.2, and $f(E)$ is the Compton scattering amplitude given by the Klein-Nishina function [8]. For a compound of more than one element, the coefficient is simply the mass-weighted summation of the individual coefficients, $\frac{\mu}{\rho} = \sum_i w_i \frac{\mu_i}{\rho_i}$ where w_i is the fraction by weight of the particular element in the compound.

We must also consider the efficiency of our phosphor system. Not every x-ray that strikes the phosphor will be converted into a photon, and every x-ray that does eventually get converted may generate many visible photons. The processes involved with the creation of these visible photons are not easily characterizable, and the interactions they undergo before leaving the phosphor are not straightforward, either. What we do instead of calculating all of this is to assign the phosphor an efficiency η that characterizes all of the phenomena associated with the creation and transport of the visible photons. We set

$$N_{ph} = \frac{\eta E}{E_{vis}} \quad (3.2)$$

where E_{vis} is the energy of the visible photons emitted, E is the energy of the x-rays being used, and N_{ph} is the number of photons emitted [9]. We can then use this theoretical number N_{ph} to make estimates for the exposure time of the film.

Chapter 4

Crystallographic Considerations

The Cool-X source would provide a conveniently small educational x-ray diffractometer should it prove capable of doing so. Here we evaluate the needs of x-ray crystal diffraction with respect to our current setup.

4.1 Crystal Basics

It is necessary to clarify some crystallographic basics before we discuss how we plan to get any crystal images out of the system. To start with, we must imagine a crystal not as a repeating pattern of ions and molecules and electrons, but as a regularly spaced lattice of points. These points are separated in space by position vectors \mathbf{a} , \mathbf{b} , and \mathbf{c} . Every lattice point is uniquely defined from the lattice origin by the position vector $\mathbf{r} = n'_a \mathbf{a} + n'_b \mathbf{b} + n'_c \mathbf{c}$. If n'_i is an integer, then the point in question lies on a lattice point, one point in a three dimensional grid formed by repeated translation of a point in steps of \mathbf{a} , \mathbf{b} , and \mathbf{c} . If n'_i is not an integer, we can rewrite \mathbf{r} so that it is the sum of lattice points and fractions of the lattice spacings.

The representation of planes in this system is fairly straightforward; we assign the planes a value corresponding to where in a given lattice cell the plane crosses the three axes. If we express these values as fractions of the axial lengths, we can describe a plane in a unit cell without talking about its physical dimensions. However, if a plane is parallel to a crystallographic axis, we have a problem; we have to describe

the intercept as being at infinity. We define the Miller index as the reciprocal of the fractional intercept, thereby eliminating the problem of our intercept being at infinity.

The spacing between two parallel planes is unique to the shape of the crystal, but follows the form of

$$\frac{1}{d_{hkl}^2} = \frac{h^2}{a^2} + \frac{k^2}{b^2} + \frac{l^2}{c^2} \quad (4.1)$$

where h, k , and l are the Miller indices of the plane for an orthorhombic system. The orthorhombic system is a generalization of the cubic system, the simplest cubic system to analyze.

It is important to keep in mind that these lattice structures are purely mathematical constructs; they are important only in that real-life crystals exist in the same type of structures as lattices make up. Crystals and lattices share symmetrical similarities, and so the study of a lattice tells us much about the workings of a crystal. We will expand upon the lattice properties further as the need for them increases.

4.2 Bragg Equation

In Section 4.1, we introduced the idea of having a periodic system of atoms arranged in a repeating pattern in space. It has been experimentally well known since the 1890's that the spacing for this lattice falls in the region of a couple Å. It was also known that x-rays have wavelengths on the order of a couple Å. In 1912, von Laue discovered that x-rays could diffract through a regular crystal, treating each atom as a new scattering center. Later that year, Bragg derived how to arrive at this same conclusion with the simple case of reflecting x-rays off of a plane [13]. It is the approach of Bragg that has seen more use since the 1912's, and it is this approach that we will use to derive the scattering conditions here.

We imagine two parallel rays (rays 1 and 2 in Figure 4-1) striking two parallel planes (P1 and P2) and scattering at an angle θ . The scattering mechanism itself consists of electrons at points O and C oscillating in response to the incoming radiation and re-emitting that radiation. The radiation is emitted isotropically, so we will typically not see any coherence between rays 1' and 2'. However, we are interested

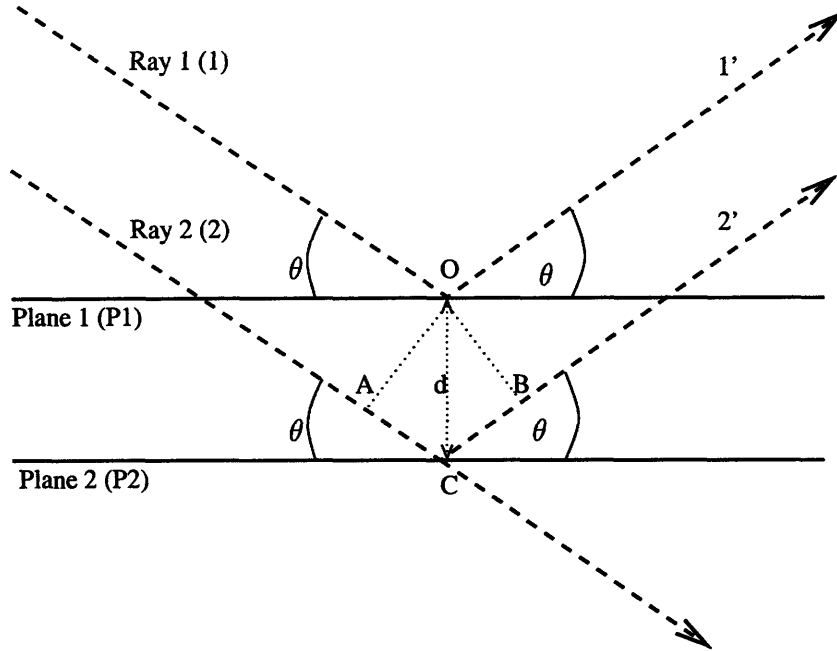


Figure 4-1: Diagram to illustrate variables used in the derivation of Bragg scattering.

in the special case where rays 1' and 2' are scattered from the parallel planes at an equal angle θ .

Looking at the perpendicular between points O, A, and B, it becomes obvious that $\angle AOC = \angle BOC = \theta$, and that therefore $AC = BC$. The waves in ray 2' will be in phase with those in 1' if the path length difference between them is an integer multiple of the wavelength of the radiation. Thus $AC + BC = n\lambda$, or using the fact that $AC/d = \sin \theta$ we get

$$2d \sin \theta = n\lambda \quad (4.2)$$

which is the famous Bragg equation [13]. For a more general three-dimensional proof of this see [7]. It is important to note that what is most commonly measured is actually the angle 2θ , as that is the angle between the initial x-ray beam and the scattered rays.

In Equation 4.2, n is the order of reflection. By rewriting d in terms of the Miller indices of our lattice, it is possible to view the reflection as first order off of a set of

planes with indices (hkl) , transforming Equation 4.2 to

$$2d(hkl) \sin \theta(hkl) = \lambda. \quad (4.3)$$

If we only get scattering off of two planes, we would expect to see very broad maxima occurring on our recording device. In a macroscopic crystal, we get thousands of planes reflecting, and so the maximum occurs at a very sharp value of θ . Diffraction patterns in a real crystal often are only tenths of a degree away from what we would expect from Bragg scattering [7].

One factor in the measurement of θ is how precise we can make our measurements. If we use 4.3 at a fixed value of λ with a width of $\sigma\lambda$, where we approximate the FWHM as the standard deviation of our source, we get that the

$$\Delta\lambda = 2d \cos \theta \Delta\theta \Rightarrow \Delta\theta = \frac{\Delta\lambda}{2d \cos \theta} \quad (4.4)$$

Using Equation 4.3, we get that

$$\Delta\theta = \frac{\Delta\lambda}{\sqrt{4d^2 - \lambda^2}} \quad (4.5)$$

Equation 4.5 gives us a parameter for determining just how well we can ever hope to get diffraction at a particular θ at a certain λ .

The fact that we get reflection off of crystal planes allows us to look at the individual characteristics of the planes within a crystal and determine physical properties of them, like the interplanar spacing d . In a similar manner to Equation 4.5, we find that the variance of any measured d is

$$\sigma_d = d \sqrt{\left(\frac{\Delta\lambda}{\lambda}\right)^2 + \left(\frac{\cos \theta \Delta\theta}{\sin \theta}\right)^2} \quad (4.6)$$

We can also do things like determine the orientation of various planes, look for imperfections in the crystal, and, last but not most certainly not least, derive a structure for the crystal we are looking at. These procedures require mapping the planes

recorded as dots on our film to various maps and “nets” of a sort, both of which are beyond the scope of this experiment.

4.3 Methods of Diffraction

In Equation 4.3, our three parameters are the interplanar spacing d , the reflection angle θ , and the wavelength λ of our radiation. There are three methods of diffraction open to us, depending on what variables we wish to vary. If we want to keep θ fixed and vary λ , we can use Laue diffraction. If we want to keep λ fixed and vary θ , there are two options. We can use the rotating-crystal approach or we can use the powder diffraction method. The rotating-crystal method has physics identical to those of the Laue method, only with a monochromatic x-ray source. We must rotate the crystal to fulfill the Bragg equation, but the same resulting patterns of diffracted spots will emerge. For further discussion of the rotating-crystal method, see [4, 7].

The Laue method consists of mounting a crystal in the path of an x-ray beam consisting of many wavelengths, often referred to as “white” radiation. By doing this, you fix the Bragg angle for every set of planes in the crystal, and the planes with the appropriate d and at the right angle θ will diffract the appropriate wavelength, resulting in a set of dots on the photographic film used. The film can either be placed between the source and the crystal or after the crystal. A transmission photograph results in dots that lie on ellipses or hyperbolas aligned along the zone axis of the reflecting plane (see Figure 4-2(b)). A zone is a set of crystal faces that share common directions, or that have planes pointing in the same direction. The zone axis is the axis that all planes in a zone are parallel to. The back-reflection results in hyperbolic arrangements aligned along zone axes.

Another method of interest is the powder diffraction method. True to its name, this method involves using either a powder of a crystal or a consolidation of randomly oriented crystal grains. What this does is allows for a variety of planes to be imaged with a single wavelength of radiation. What happens is that for certain particles in the powder, the reflecting planes are positioned correctly for the wavelength of light

hitting them. And because we have a large number of particles in our sample, we have every possible angle of incidence covered. For those angles that obey the Bragg equation, we get constructive interference. What this results in is a series of cones being projected from the sample, each cone being the result of Bragg scattering at a particular θ . If we were to place this powder sample in front of a recording screen, we would see rings forming at the values of θ that fulfilled the Bragg equation. We would actually measure 2θ , as this is the total deviation from the incoming x-ray beam. See Figure 4-2(a) for an illustration. A subset of the powder method is the Hull/Debye-Scherrer method, where a cylindrical film is used to record the rings formed by the Bragg-diffracted x-rays. This avoids some problems inherent with the flat screen, namely the obliqueness of the angle formed with the film. This contributes a factor of $\frac{1}{\cos \theta}$ to the width of the rings observed. This makes Equation 4.5 into

$$\frac{\Delta\theta}{\cos \theta} = \frac{\Delta\lambda}{2d} \quad (4.7)$$

which describes the width of any lines that appear on our flat screen recording media.

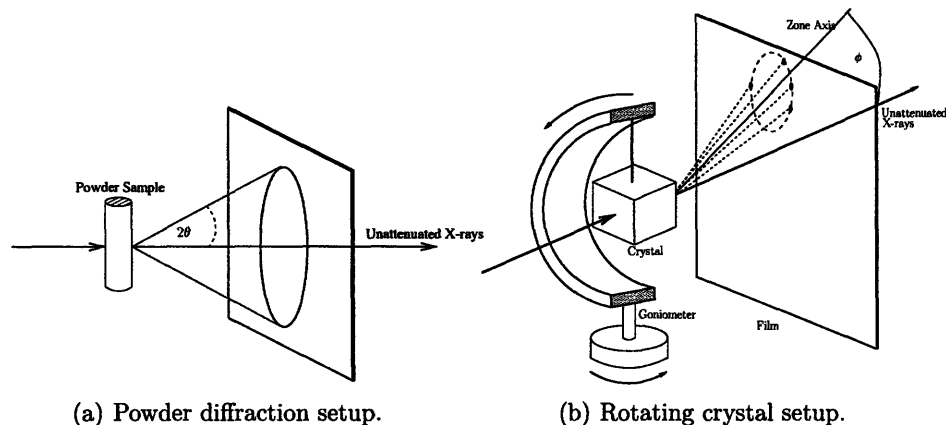


Figure 4-2: Different methods of x-ray diffraction.

The powder method has the advantage over the Laue method in that our current setup has two prominent wavelengths, the $\text{Cu K}\alpha$ and $\text{K}\beta$ lines, and so would work better with the equipment we already possess. However, any attempts to get an image will be done in the style of a rotating crystal, as our spectrum has a strongly

monochromatic nature, and the crystals available to use are in a cohesive, non-powder form. The rotating crystal transmission photograph is also useable as a method of crystal orientation, and the powder diffraction method is completely unable to do so, as we're not even using a crystal. The pure Laue method is unattainable, as we do not have a very good white radiation source. However, the physics of the Laue method and the projections needed to extrapolate crystal properties are exactly the same in the rotating crystal method, with only slight modifications, and so we can use the physics of the two interchangeably.

Chapter 5

Results

5.1 Experimental Setup

The Cool-X source, by itself and in combination with the X-123 spectrometer, is a good tool for the study of x-ray spectra and absorption. One could set up and run an experiment to calculate the absorption coefficient of various materials by placing them between the source and the detector and comparing the rate of x-ray detection as a function of the attenuator. There would be some difficulty with this, as the output of the source is not constant, and so a long integration period would be necessary in order to smooth out the count rate.

This experiment was not performed, as the ability of the source to perform in this function is not in doubt. The main experiment performed with the Cool-X was to see if the source was suitable for x-ray diffraction. The setup for this experiment was as follows.

The entire experiment was enclosed in 1/2" thick leaded acrylic with .5mm lead equivalent. The box was joined at the edges with stepped edges. This allowed us to make sure none of the joints could result in a radiation leak if the edges separated. This shielding was more than enough to stop the scattered x-rays from the experiment, as well as any of the primary beam that penetrated through the film cassette. Even though our source, with its peak at $\approx 8\text{keV}$, lacked much penetrating power, it was still necessary to shield our experiment. The maximum exposure from our source was

about 2 mCi, high enough that we want to shield ourselves. Although a low level, we want to follow the ALARA (As Low As Reasonably Achievable) practices.

The source and detector were mounted on optical rails using post holders and mounting plates fashioned in-house. These plates were fashioned in such a way as to have the source pointing directly down the main axis of the optical rail, for the convenience in aligning the X-123 spectrometer when it was used.

Our system was collimated according to the guidelines in Section 2.2. The collimator diameter d was 5mm, the collimator length u was 20mm, the collimator to source distance v was 2.7cm, and the collimator to crystal distance w was 0, that is, whenever we used a crystal, it was placed directly at the opening of the collimator. This was done to preserve the x-ray flux coming out of the collimator, as the beam was low enough in counts without letting it spread even further. The dimensions resulted in a maximum divergence angle of 14.3 degrees.

Our source had a radius of 4.5mm and, for simulation purposes, was modeled as being uniform in intensity in the forward direction.

The phosphor screen used for this investigation was a Lexel Imaging Solutions, Inc. model PLGDXTB-20 screen 3"×3" square on a .15mm clear Mylar backing. The model PLGDXTB-20 is a $\text{Gd}_2\text{O}_2\text{S:Tb}$ type phosphor with an emission maximum at 540nm [9]. This phosphor was kept at a distance of $\approx 1\text{mm}$ from the film during experimentation. Using Equation 3.1, the linear attenuation coefficient $\mu_{P43} = 2.39 \times 10^3 \text{cm}^{-1}$. Our phosphor has an active element thickness of $80\mu\text{m}$, and so using $I = I_0 \exp^{-\mu_{P43}x}$ we get that $\frac{I}{I_0} = 5 \times 10^{-9}$, which makes sense because the x-rays travel through ≈ 19 mean free paths in $80\mu\text{m}$ of $\text{Gd}_2\text{O}_2\text{S:Tb}$. This means that our phosphor has a stopping power of our energy x-rays of nearly one. This is good in that we converted many of these into visible photons for interaction with our film.

The film we used was Polaroid Type 59 Polacolor ER. This film has an ISO of 80, corresponding to a relatively slow exposure time for visible light. The film was used in conjunction with a Polaroid Land film holder #500. This was necessary to use, as the Polaroid film was processed using the envelope the film was stored in. This was extremely convenient, as we could remove the film from the x-ray beam and pull it

out of the housing, instantly processing the film.

The crystals that were used to attempt diffraction studies were CaF_2 and malonic acid. The CaF_2 was obtained from a geode and cut with a razor blade and hammer to a width of 3mm on a side and a thickness of .5mm. The malonic acid crystal was soft enough to cut with minimal pressure. The size of this crystal was the same as the CaF_2 crystal. They were both mounted on quartz rods with the aid of an epoxy glue. In the future, samples should be mounted on glass or another amorphous solid so we don't get any accidental diffraction from the crystalline quartz.

The crystals could be mounted on a two-axis goniometer. This goniometer was designed so that a specific crystallographic axis, such as the growth axis, of a particular crystal could be aligned parallel to the x-ray beam and the crystal could be rotated about two axes perpendicular to the beam axis. This would allow the acquisition of Laue patterns at specific angles, the data of which could be used to confirm the predicted results of diffraction theory.

5.2 Experimental Procedure

All exposures presented in this section are the result of 80 minute source exposure times. Distances from the collimator and other pertinent information are given with the particular photograph. See Figure 5-1 for a picture of the laboratory setup.

The Polaroid Land film holder was covered in optically opaque black film in order to make the cassette light-tight. This was to avoid any unwanted optical photons from exposing the film.

Any crystals used in this process were inspected with a polarizing stereomicroscope, to show that they are indeed single crystals. The CaF_2 crystal faces were aligned by eye.

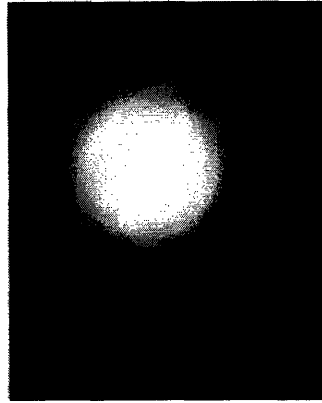


Figure 5-1: Picture of the desktop setup for the experiments. Seen are the collimated Cool-X source, the X-123 spectrometer, and the goniometer mount in back.

5.3 Experimental Results

What we have attempted to demonstrate is that, using a collimator and a system of recording media, we can use the Cool-X source as a source for x-ray diffraction. We had hoped that this would result in an experimental validation of Bragg's law (Equation 4.2). With a properly aligned crystal and a sufficiently collimated source, we were hoping to detect evidence of Bragg scattering in the form of a blurring or, if all went well, actual diffraction rings or spots. What we saw after exposure, however, was not what we were hoping for.

Figure 5-2(a) shows what happens to our film upon direct exposure to our x-rays. We see that our x-rays will expose our film. There are artifacts along the bottom right side of the image from a small opening in the light-tight enclosure. This 80 minute exposure without the collimator was taken at a distance of 5mm from the



(a) Example exposure of Polaroid type 59 optical film. This is an 80 minute exposure at point blank range (5mm source to film) with no collimator and no phosphor screen.



(b) Example exposure of Polaroid type 59 optical film with the phosphor screen in place. This is an 80 minute exposure with a the phosphor screen 1mm from the film and the source 5mm from the film.



(c) An example of the data measured with no phosphor screen and a collimator with a diameter of 5mm. The collimator was 5mm from the film. Exposed section is in top half of the picture



(d) The result of exposing the phosphor screen with collimated radiation. The collimator was placed 5mm from the film and 4mm from the phosphor. There is no exposure due to the phosphor.

Figure 5-2: Sample exposures of Polaroid type 59 film to the Cool-X source. All figures are at the same scale.

source, as this was as close as the film holder would allow. This picture served as the baseline photograph for our investigation.

Figure 5-2(b) shows the same setup as Figure 5-2(a), only with the phosphor screen positioned 1mm away from the film itself. This shows us something a little surprising; the phosphor appears to be reducing the exposure of our film. This was not initially expected, but there is a very good explanation for this.

This decrease in intensity can be explained by looking at where in the phosphor the x-rays get absorbed. Using Equation 3.1, we see that the linear attenuation coefficient for our $\text{Gd}_2\text{O}_2\text{S:Tb}$ is $2.39 \times 10^3 \text{cm}^{-1}$, which corresponds to a mean free path (distance at which one half of x-rays have interacted) of $4.18\mu\text{m}$. This is the source of our phosphor troubles. Half of the x-ray interact in the first $4\mu\text{m}$, only a quarter remains after $8\mu\text{m}$. After traversing the $80\mu\text{m}$ thickness, the beam has had to travel through almost 20 mean free paths. The vast majority of our x-rays were stopped within 4 or 5 mean free paths.

This seems like a good thing; the phosphor stops nearly all of our x-rays, so the efficiency of our system should increase dramatically. And, using the published value of $\eta \approx 14.5\%$ [9] in Equation 3.2, we see that every x-ray absorption event should create around 500 photons. Again, this should drastically help to increase our overall system efficiency. It would do so, but unfortunately for us, our phosphor is optically opaque. This means that when the photons are emitted from x-ray interaction, they're mostly absorbed before they can make it out the other side of the phosphor screen. So while we are creating a great number of visible photons, they are being reabsorbed before they are able to strike the Polaroid film.

We see this loss of signal in Figures 5-2(c) and 5-2(d). Figure 5-2(c) shows the film after an 80 minute exposure with the collimator and no phosphor, and Figure 5-2(d) shows the film after an 80 minute exposure with the phosphor. The small amount of signal in Figure 5-2(c) was not enough to illustrate any crystallographic properties, and so we had hoped to increase the signal. As is apparent in Figure 5-2(d), this did not happen. Therefore the experiment was unsuccessful at producing crystallographic features of x-ray diffraction.

Chapter 6

Conclusions

We have shown that, with the experimental setup presented, Bragg diffraction is not observable. Although our film exposed to both visible photons and x-rays, we were unable to get enough exposure to make any real measurements. This was due to the absorption of our visible photons within the phosphor screen, lowering the system efficiency drastically even as we created more potential signal through the use of our phosphor screen.

Although we were unable to observe Bragg scattering, that does not mean that our system is unable to function as a diffractometer. There are changes that could be made to our system in order to help raise our overall efficiency.

The largest change comes in the form of a different phosphor screen. Instead of our current $\text{Gd}_2\text{O}_2\text{S:Tb}$ screen, we could use a less attenuating phosphor, $\text{Gd}_2\text{O}_2\text{S:F}$. This would allow us to maintain the same setup as previously while decreasing the number of mean free paths the x-rays would traverse.

In a similar vein, We could also use a thinner scintillator. We wouldn't have to change materials if we had a phosphor screen that was $4\mu\text{m}$ (1/20th our current thickness). If a commercial supplier could be found that could manufacture such a screen, then the efficiency of our system would drastically increase.

Another way to increase the amount of visible photons available is to do a "sandwiching" diffraction experiment. Instead of positioning the film after the sample and scintillator, we instead place it in front of our sample. We could drill holes through

the film and film holder to allow the passage of the x-rays through the apparatus without attenuation. We would hope to record Bragg diffraction incidents as the x-rays passed through the crystal, scattered, and struck the scintillator, which would then re-radiate in the visible spectrum. As we are now placing our film close to the active surface of the sample, we now hope to see the effects of Bragg scattering. We would have to ensure that the distances between scintillator and film were not so drastic as to destroy the resolution of our system.

The major obstacle to this experiment right now is a lack of a film holder that we can feel free to drill through. The film holder being used currently is property of the MIT Technique, and so placing holes in it is out of the question. However, such an experiment, if performed, could very well produce evidence of Bragg diffraction.

If we were to perform this experiment from scratch, one piece of equipment that has the potential for improving our signal strength is a CCD camera. If we had a sufficiently large fiber optic taper with the larger end coated with a thin ($10\mu\text{m}$) x-ray phosphor, the gains in our signal would be immense. Because the CCD functions in real time, we would be able to do rotating crystal diffraction with ease. You could position your sample, turn on the source, wait for three or four heating cycles (around 5 minutes), yielding ≈ 22500 x-rays within 200eV of the copper $K\alpha$ line at .041keV. With a reasonably efficient (50% or so) CCD/phosphor system, we could reasonably expect to be able to cover 90 degrees of rotation, with 5 degree rotations, in an hour and a half.

While our experiment was unsuccessful at showing Bragg diffraction, we have shown that our system is an excellent source for the study of x-ray properties. We cannot show Bragg diffraction with our current experimental setup, but there are yet options available for us to continue to attempt to show diffraction.

Appendix A

Bragg Interference

One interesting question not pertaining directly to this work is the question of whether the fundamental idea behind using the Bragg equation is actually valid. We made the leap from saying that the Bragg equation is correct for two scattering centers to saying that it implied that reflection off of planes occurs. This result is not obvious in the mathematical methods we initially used. It is a result of a three-dimensional scattering problem, but we did not analyze the problem as such. Therefore we need to prove to ourselves that this reflection phenomenon is actually valid. We shall do so in a two-dimensional case which can be easily extrapolated to three dimensions. This follows the derivation in [13].

Take three non-collinear points A , B , and C which all separately scatter an incoming beam in a direction that results in constructive interference (see Figure A-1). We know that for constructive interference, the difference in path length must be an integer multiple of the wavelength, so we see that

$$\begin{aligned} a - b &= h\lambda \\ c + d &= k\lambda \end{aligned} \tag{A.1}$$

where h and k are integers. We then assign the angles of incidence and reflection from the line AB (plane AB , more appropriately) the values of ψ and ψ' . Note that these values are not always equal. If x is the distance between points A and B , and

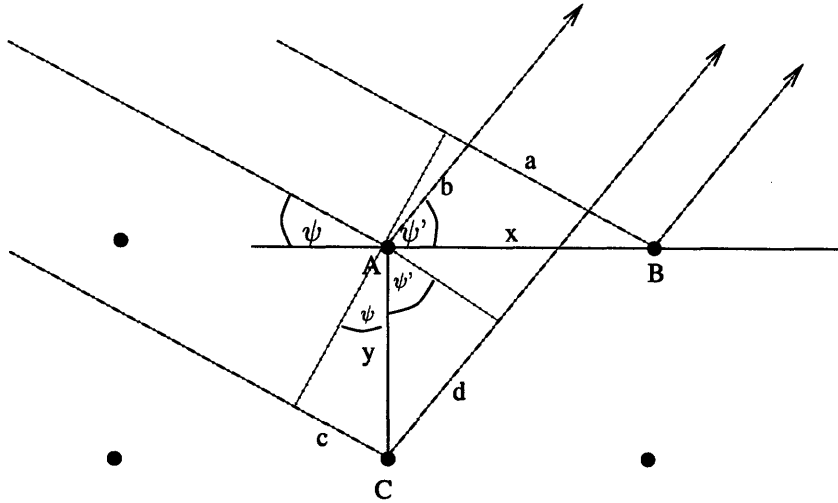


Figure A-1: Parallel x-ray scattering off of three lattice points.

y is the distance between A and C , Equation A.1 becomes

$$\begin{aligned} x \cos \phi - x \cos \phi' &= h\lambda \\ y \sin \phi + y \sin \phi' &= k\lambda \end{aligned} \quad (\text{A.2})$$

We now look at a different plane drawn through our system, plane RS (see Figure A-2). We draw the plane so that it has an equal angle θ from the scattered and incident beams and an angle α with AB .

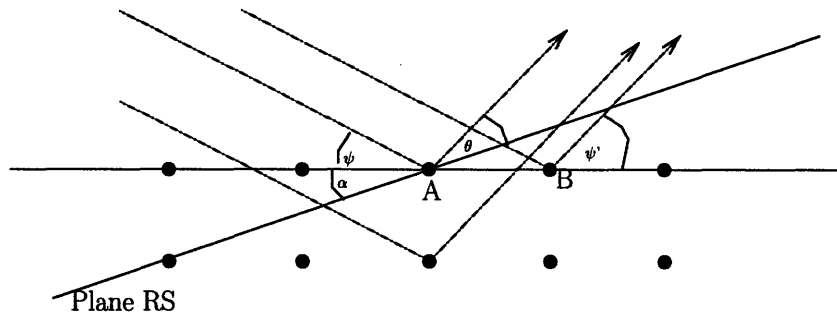


Figure A-2: Lattice plane RS reflection.

This gives us that $\theta = \psi + \alpha = \psi' - \alpha$. We rearrange to get ψ and ψ' and rewrite

Equation A.2 as

$$\begin{aligned}x [\cos(\theta - \alpha) - \cos(\theta + \alpha)] &= h\lambda \\y [\sin(\theta - \alpha) + \sin(\theta + \alpha)] &= k\lambda\end{aligned}\tag{A.3}$$

Expanding this with trigonometric functions leads us to

$$\begin{aligned}2x \sin \theta \sin \alpha &= h\lambda \\2y \sin \theta \cos \alpha &= k\lambda\end{aligned}\tag{A.4}$$

leading us to

$$\tan \alpha = \frac{hy}{kx}\tag{A.5}$$

The interpretation of Equation A.5 is that as RS passes through A, it travels repeatedly through lattice points shifted h in the y direction and k units in the x direction. This is simply a lattice plane (h,k) . This leads us to conclude that the conditions for constructive scattering corresponds to reflection off of a lattice plane of the correct orientation. We have now shown that the Bragg equations truly represent reflection off of a plane, and may rest easy knowing that our assumptions in Chapter 4 are valid.

Bibliography

- [1] Amptek Inc. *Amptek Complete X-Ray Spectrometer X-123*, 2006.
- [2] Amptek Inc. *Cool-X X-ray Generator with Pyroelectric Crystal Operating Manual*, 2006.
- [3] Zang-Hee Cho, Joie P. Jones, and Manbir Singh. *Foundations of Medical Imaging*. John Wiley and Sons, Inc., 1993.
- [4] B.D. Cullity and S.R. Stock. *Elements of X-Ray Diffraction*. Prentice Hall, third edition, 2001.
- [5] M. Deutsch, G. Hölzer, J. Härtwig, J. Wolf, M. Fritsch, and E. Förster. $K\alpha$ and $K\beta$ x-ray emission spectra of copper. *Physical Review A*, 51(1):283–96, January 1995.
- [6] J.H. Hubbell and S.M. Seltzer. Tables of x-ray mass attenuation coefficients and mass energy-absorption coefficients. Technical report, NIST, Gaithersburg, MD, 2004. Version 1.4. [Online] Available <http://physics.nist.gov/xaamdi> [2007, May 9].
- [7] Harold P. Klug and Leroy E. Alexander. *X-Ray Diffraction Procedures*. John Wiley & Sons, Inc., 1953.
- [8] Albert Macovski. *Medical Imaging Systems*. Information and Systems Science Series. Prentice-Hall Inc., 1983.
- [9] Martin Nikl. Scintillation detectors for x-rays. *Measurement Science and Technology*, 17:R37–R54, 2006.

- [10] E.T. Peters and S.A. Kulin. Experimental considerations for polaroid film x-ray photographs. *The Review of Scientific Instruments*, 37(12):1726–29, December 1966.
- [11] Wilhelm Conrad Röntgen. On a new kind of ray. *Science*, 3(59):227–31, February 1896.
- [12] H.G. Smith. Use of polaroid film in neutron and x-ray diffraction. *The Review of Scientific Instruments*, 33(1):128–29, January 1962.
- [13] George H. Stout and Lyle H. Jensen. *X-ray Structure Determination: A Practical Guide*. Wiley-Interscience, second edition, 1989.